Supporting Information

Bottlebrush bridge between soft gels and firm tissues

Andrew N. Keith,[1] Mohammad Vatankhah-Varnosfaderani,[1] Charles Clair,[2] Farahnaz Fahimipour,[1] Erfan Dashtimoghadam,[1] Abdelaziz Lallam,[2] Michael Sztucki,[3] Dimitri A. Ivanov,[4,5,6] Heyi Liang,[7] Andrey V. Dobrynin,[7*] Sergei S. Sheiko[1*]*

[1]Department of Chemistry, University of North Carolina at Chapel Hill, 27599, USA

[2]Université de Haute Alsace, Laboratoire de Physique et Mécanique Textiles, 11 rue Alfred Werner, F-68093 Mulhouse Cedex, France

[3]European Synchrotron Radiation Facility, F-38043 Grenoble, France

[4]Institut de Sciences des Matériaux de Mulhouse-IS2M, CNRS UMR 7361, 15, rue Jean Starcky, F-68057 Mulhouse, France

[5]Lomonosov Moscow State University, Faculty of Fundamental Physical and Chemical Engineering, Leninskie Gory 1/51, 119991, Moscow, Russian Federation

[6]Institute of Problems of Chemical Physics, Russian Academy of Sciences, Chernogolovka, Moscow region, 142432, Russian Federation

[7]Department of Polymer Science, University of Akron, Ohio, 44325-3909, USA

S1. Effect of nonlinear deformation of bottlebrush blocks on domain structure and network elastic properties.

Equilibrium Domain Spacing. Consider an LBL triblock copolymer consisting of linear *L*-blocks with the degree polymerization (DP) n_L and bottlebrush B-block with backbone DP n_{bb}. In the bottlebrush block, side chains with DP n_{sc} are attached to every monomer of the backbone such that the number of bonds between neighboring grafting point is n_g=1. The properties of the linear *L*-chains are characterized by the bond length (monomer projection length) l_L, Kuhn length b_L and monomer pervaded volume v_L. For bottlebrush *B*-block, we assume that backbones and side chains are made of identical monomers with bond length l_B, Kuhn length b_B and monomer pervaded volume v_B. Interactions between side chains stiffen bottlebrush blocks such that the effective Kuhn length of the bottlebrush block b_k depends on the value of the crowding parameter, Φ, describing the degree of mutual interpenetration between side chains and backbones of the neighboring bottlebrush macromolecules.[31] The crowding parameter depends on the monomer excluded volume v_B, bond length l_B, Kuhn length b_B, DP of the side chains n_{sc} and volume fraction of the backbone monomers

$$\varphi = \frac{n_g}{n_g + n_{sc}} \qquad (S.1)$$

and has the following form

$$\Phi \approx \frac{v_B}{(l_B b_B)^{3/2}} \frac{\varphi^{-1}}{n_{sc}^{1/2}} \qquad (S.2)$$

For bottlebrush macromolecules the effective Kuhn length scales linear with the crowding parameter such as

$$b_K \approx b_B \Phi/\Phi^* \qquad (S.3)$$

The crossover value of the crowding parameter $\Phi^* \approx 0.7$ was determined from analysis of the renormalization of the effective Kuhn length of graft polymers in a melt.[31]

The composition of the triblock copolymers is characterized by the volume fraction of the *L*-blocks which is defined as follows

$$\phi_L = \frac{2v_L n_L}{2v_L n_L + v_B\left(n_{bb} n_{sc}/n_g + n_{bb}\right)} = \frac{2v_L n_L}{2v_L n_L + v_B n_{bb}/\varphi} \qquad (S.4)$$

This defines the bottlebrush elongation ratio or the equilibrium distance between spherical aggregates as a function of the molecular parameters in the case of the nonlinear deformation of the bottlebrush block.

Flory-like calculations of equilibrium size $2L_B$ of the bottlebrush block connecting spherical domains of the linear *B*-blocks of the microphase separated immiscible *L*- and *B*-blocks results in the following nonlinear relationship[34]

$$\beta^{3/2}(1+2(1-\beta)^{-2}) = Cd\left(\frac{R_{gl}}{R_{max}}\right)^3 \frac{\gamma_{LB} b_K R_{max}}{k_B T} \qquad (S.5)$$

for the bottlebrush block elongation ratio

$$\beta = 4L_B^2/R_{max}^2 \qquad (S.6)$$

where Cd is a numerical constant which value depends on the symmetry of the domain structure, γ_{LB} is the surface tension of the *LB*-interface, $R_{gl} = \left(3v_L n_L / 4\pi\right)^{1/3}$ is the size of the collapsed linear block, $R_{\max} = l_B n_{bb}$ is the size of the fully extended bottlebrush backbone, k_B is the Boltzmann constant and T is the absolute temperature.

Deformation of Self-Assembled Bottlebrush Networks. The deformation of a polymer network undergoing uniaxial deformation is described by the following constitutive equation relating true stress with the network elongation ratio λ:[6,18]

$$\sigma_{true} = \frac{E}{9}(\lambda^2 - \lambda^{-1})\left(1 + 2\left(1 - \frac{\beta I_1(\lambda)}{3}\right)^{-2}\right) \qquad (S.7)$$

where $I_1(\lambda) = \lambda^2 + 2/\lambda$ is the first deformation invariant. The structural Young's modulus E and strand elongation ratio β are determined by the molecular architecture of the network strands and their concentration. For incompressible networks the structural shear modulus is related to the structural Young's modulus E as $E = 3G$. The bottlebrush block elongation ratio β is given by eq S.6. Structural Young's modulus of the network, E, is defined as

$$E \approx C_1 k_B T \frac{\rho_B \varphi}{n_{bb}} \frac{R_{max}}{b_K} \beta(1-\phi_L) \qquad (S.8)$$

where C_1 is a numerical constant on the order of unity accounting for a network topology.

It is important to point out that the structural modulus is different from the Young's modulus at small deformations ($\lambda \to 1$)

$$\left.\frac{d\sigma_{true}}{d\lambda}\right|_{\lambda=1} = E_0 = \frac{E}{3}(1+2(1-\beta)^{-2}) \qquad (S.9)$$

Thus, using equation S.8 and S.5 we find the following scaling relation for the Young's modulus at small deformation in terms of the molecular parameters[34]

$$E_0 \approx \frac{\gamma_{LB} R_{gl}^3}{R_{max}} \frac{\rho_B \varphi}{n_{bb}} (1-\phi_L)\beta^{-1/2} \qquad (S.10)$$

Eq S.10 shows a good agreement with the experiment (fig. 3c).

Table S1: Mechanical parameters of tissues. All tissues are represented in Fig. 1d and Fig. 3b with highlighted entries selected for Fig. 1a.

Label	Tissue	$E\ (Pa)$ [1]	β [1]	$E_0(kPa)$ [2]	Ref
1	Porcine aorta	19800	0.67	127.8	35
2	Dog lung	300	0.69	2.2	36
3	Brain	60	0.75	0.7	37
4	Blood vessel	3400	0.75	37.4	38
5	Fetal membrane	1300	0.79	20.1	39
6	Lens capsule	10800	0.90	723.6	40
7	Heart muscle	20	0.96	8.3	41
8	Human abdominal skin	1200	0.93	163.7	42
9	Eel skin	7800	0.84	205.7	43
10	Mice skin	2600	0.90	174.2	44
11	Porcine skin parallel spine	5800	0.74	59.1	45
12	Porcine skin perpendicular spine	10600	0.46	27.8	45
13	Human alveolar wall	84	0.87	3.3	46
14	Human vocal fold ligament	147	0.93	20.0	47
15	Zonular filaments	69	0.92	7.2	48
16	RA muscle fiber bundle	204	0.75	2.3	49
17	Human single muscle fiber	2016	0.54	7.0	50
18	Wild turkey muscle	441	0.90	29.5	51
19	Human adipose tissue	7	0.96	3.0	52
20	Pig belly slow rate	5457	0.45	13.8	53
21	Artery adventitia A	348	0.91	28.8	54
22	Porcine meniscus	23508	0.97	17421	55
23	Thrombus	12	0.98	19.5	56
24	Invertebral disk posterior	606	0.93	82.7	57
25	Invertebral disk anterior	208	0.96	86.6	57
26	Spinal cord	2724	0.84	71.8	58
27	Porcine brain	1005	0.72	8.9	59

[1] Structural modulus E and strain-stiffening parameter β are fitting parameters in eq. 1. [2] Young's modulus at small deformations which can be determined either as tangent of a stress-strain curve at $\lambda = 1$ or from fitting equation eq. 2.

Table S2: Mechanical parameters of gels. All gels are represented in Fig. 1d and Fig. 3b with highlighted entries selected for Fig. 1b.

Label	Gel [1]	$E\ (kPa)$ [2]	β [2]	$E_0(kPa)$ [3]	Ref
1	Zwitterionic sulfobetaine	5.70	0.0041	5.7	60
2	PAM/Surfactant	6.38	0.015	6.5	61
3	PAM/Surfactant	16.5	0.036	17.3	61
4	Synthetic elastin	263.9	0.02	271.1	62
5	PDMA/Silica	1.49	0.008	1.5	63
6	PEDOT/PSS	91.5	0.128	110.7	64
7	PEDOT/PSS	30.8	0.077	34.4	64
8	PAMAP/PAM	733.2	0.219	1047	65
9	PAM	245.7	0.074	272.9	65
10	Clay nanocomposite	1.36	0.005	1.4	66
11	Bimodal PEG	2.82	0.163	3.6	67
12	Polyrotaxane	9.41	0.033	9.8	68
13	PNIPAM/Clay nanocomposite	77.1	0.005	77.5	69
14	PAM/Clay nanocomposite	1435	0.002	1438	70
15	Microfibrillated cellulose/Elastin	116.9	0.436	284.0	71
16	PAM/Xanthan Gum	140.2	0.001	140.3	72
17	PAM/Xanthan Gum	560.9	0.001	561.6	72
18	ICE PAM/Alginate	105.5	0.026	109.3	73
19	PAM/Alginate	75.8	0.259	117.4	74
20	PAM/Alginate with Cations	112.8	0.029	117.4	75
21	Iota-carrageenan/PAM	8.09	0.001	8.1	76
22	Kappa-carrageenan/PAM	23.8	0.254	36.4	76
23	PVA/PAM	74.2	-	74.2	77
24	PDGI/PAM-PAA	48.6	0.007	49.1	78
25	PDGI/PAM	44.9	0.007	45.4	78
26	PAM/PAA	2.03	0.119	2.4	78
27	Graphene/PAACA	6.58	0.042	6.9	79
28	PAACA	2.15	0.114	2.5	79
29	PNVP/PAA	12.3	0.297	20.7	80
30	PAA/SAPS	106.5	0.038	112.2	81

[1] Gel name represents the defining features and chemistry, for specifics please visit referenced literature. [2] Structural modulus E and strain-stiffening parameter β are fitting parameters in eq. 1. [3] Young's modulus at small deformations which can be determined either as tangent of a stress-strain curve at $\lambda = 1$ or from the fitting equation eq. 2.

Table S3: Structural and mechanical parameters of reported LBL PMMA-PDMS-PMMA.

Sample	n_{bb}[1]	n_L[2]	ϕ_L[3]	$E(kPa)$[4]	β[4]	$E_0(kPa)$[5]	d_3 (nm)[6]	D_L (nm)[7]	d_1 (nm)[8]
Group 1 ($n_{sc} = 14$)[9]									
300-1/14	302	57	0.030	4.5	0.48	12.8	42.9	20.8	3.44
300-2/14	302	117	0.059	5.5	0.56	20.4	45	25.5	3.45
300-3/14	302	181	0.089	5.6	0.69	41.5	45.7	30.2	3.45
600-1/14	602	295	0.074	2.9	0.30	4.9	NA	NA	NA
600-2/14	602	351	0.087	3.6	0.35	6.9	NA	NA	NA
600-3/14	602	677	0.155	4.4	0.42	10.1	NA	NA	NA
600-4/14	602	803	0.179	5.0	0.51	15.3	NA	NA	NA
900-1/14	938	190	0.032	3.3	0.29	5.4	55.5	24.3	3.48
900-2/14	938	325	0.053	3.6	0.33	6.5	59.3	32.3	3.44
900-3/14	938	656	0.102	4.7	0.45	11.8	78.8	50.9	3.42
900-4/14	938	1235	0.177	6.2	0.67	39.3	141	NA	3.43
1200-1/14	1065	360	0.052	3.3	0.26	5.1	66.4	33.4	3.56
1200-2/14	1065	480	0.068	3.8	0.30	6.4	79.1	42.8	3.56
1200-3/14	1065	810	0.110	3.9	0.36	7.8	77.4	45.7	3.55
Group 2 ($n_{sc} = 70$)[9]									
100-1/70	112	105	0.029	12.8	0.71	106.2	28.5	12.0	7.10
100-2/70	112	131	0.036	11.0	0.76	130.0	33.8	15.3	7.06
100-3/70	112	185	0.050	6.12	0.84	155.7	37.1	18.7	7.05
300-1/70	296	156	0.017	1.07	0.77	13.3	71.05	24.8	7.15
300-2/70	296	285	0.030	1.05	0.80	18.3	69.97	29.7	7.10
300-3/70	296	507	0.052	0.80	0.85	24.8	90	45.9	7.03
300-4/70	296	754	0.075	0.75	0.91	55.7	113	65.3	7.06
450-1/70	447	288	0.020	1.32	0.71	11.2	66.3	24.6	6.95
450-2/70	447	604	0.041	1.49	0.78	20.4	84.5	39.9	6.94
450-3/70	447	772	0.052	1.16	0.81	22.3	82.2	42.0	6.93
450-4/70	447	894	0.060	1.29	0.82	26.3	102.2	54.6	6.90

(1) Degree of polymerization (DP) of bottlebrush block backbone determined by ^{1}H-NMR and verified by AFM (Fig. S6,8). (2) DP of PMMA linear block by ^{1}H-NMR (Fig. S7). (3) Volume fraction of L-block calculated using $\phi_L = (2n_L M_{MMA}/\rho_{MMA})/(2n_L M_{MMA}/\rho_{MMA} + n_{bb} M_{sc}/\rho_{PDMS})$ where $\rho_{PMMA} = 1.15\ g/cm^3$, $\rho_{PDMS} = 0.96\ g/cm^3$, $M_{MMA} = 100 g/mol$ and where $M_{sc} = 1024\ g/mol$ and $M_{sc} = 5227\ g/mol$ are the respective molar masses of Group 1 and 2 macromonomers measured by NMR. (4) Structural modulus and strain-stiffening parameter obtained by fitting stress-strain curves with eq. 1. (5) Young's modulus from eq 2. (6) Position of the main interference peak (see text for details). (7) Diameter of PMMA spherical domains is determined from the form-factor of spheres (d_2). (8) Position of bottlebrush scattering caused by the electron-density contrast between the brush backbone and that of the side chains. (9) Effective DP of PDMS side chains determined as $n_{sc} = M_{sc}/M_0$ where M_0=74 g/mol is molar mass of PDMS monomer.

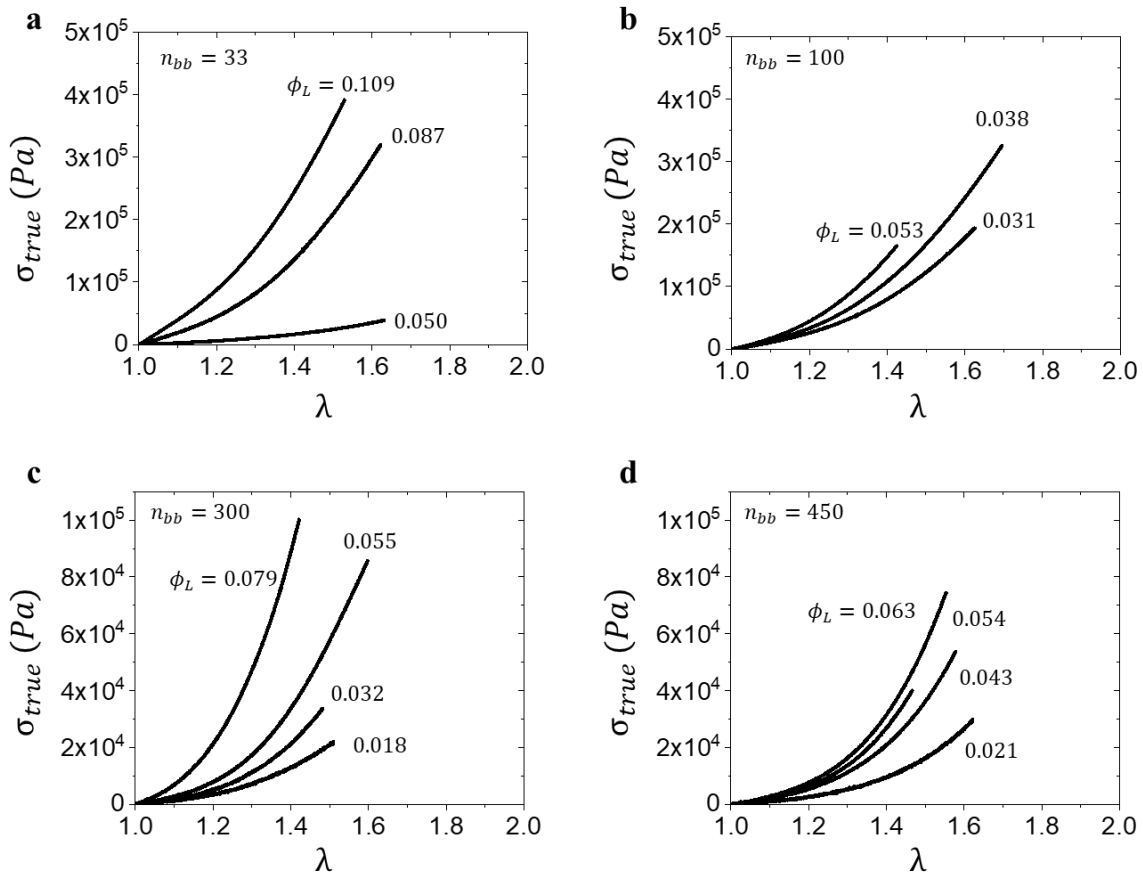

Figure S1: True stress-elongation curve profiles of n_{sc} = 70 LBL plastomer series. **(a)** 33-x/70 **(b)** 100-x/70 **(c)** 300-x/70 **(d)** 450-x/70.

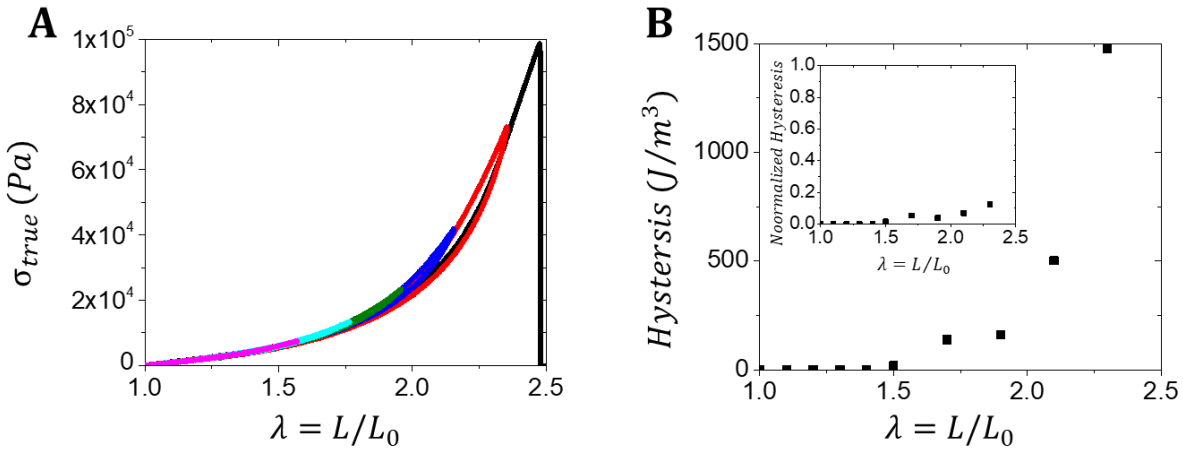

Figure S2: (A) Cyclic loading-unloading curves of 1200-3/14. Stress-strain curves reveal the emergence of a hysteresis at $\lambda \approx 0.6\lambda_{max}$. (B) Hysteresis energy as a function of elongation, inset: normalized hysteresis.

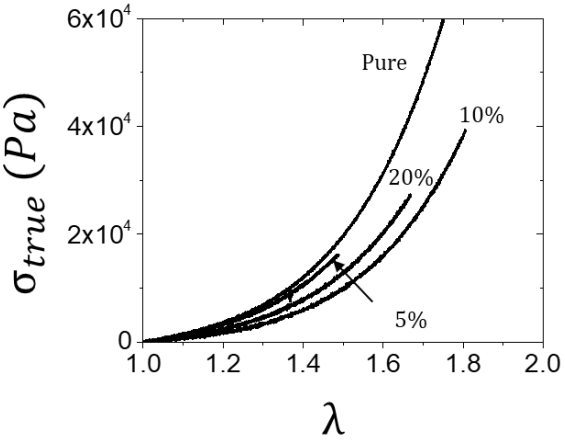

Sample [1]	λ_{fit}	$E\ (kPa)$	β	$E_0\ (kPa)$
Pure	1.3	1.6	0.718	14.5
5%	1.3	1.4	0.728	12.9
10%	1.5	1.2	0.711	9.8
20%	1.4	0.9	0.705	7.2

Figure S3: Stress-elongation curves of a pure 300/70 plastomer sample diluted with increasing weight fractions of free bottlebrush and cast from THF, which highlights decoupling E_0 and β as summarized in the table.

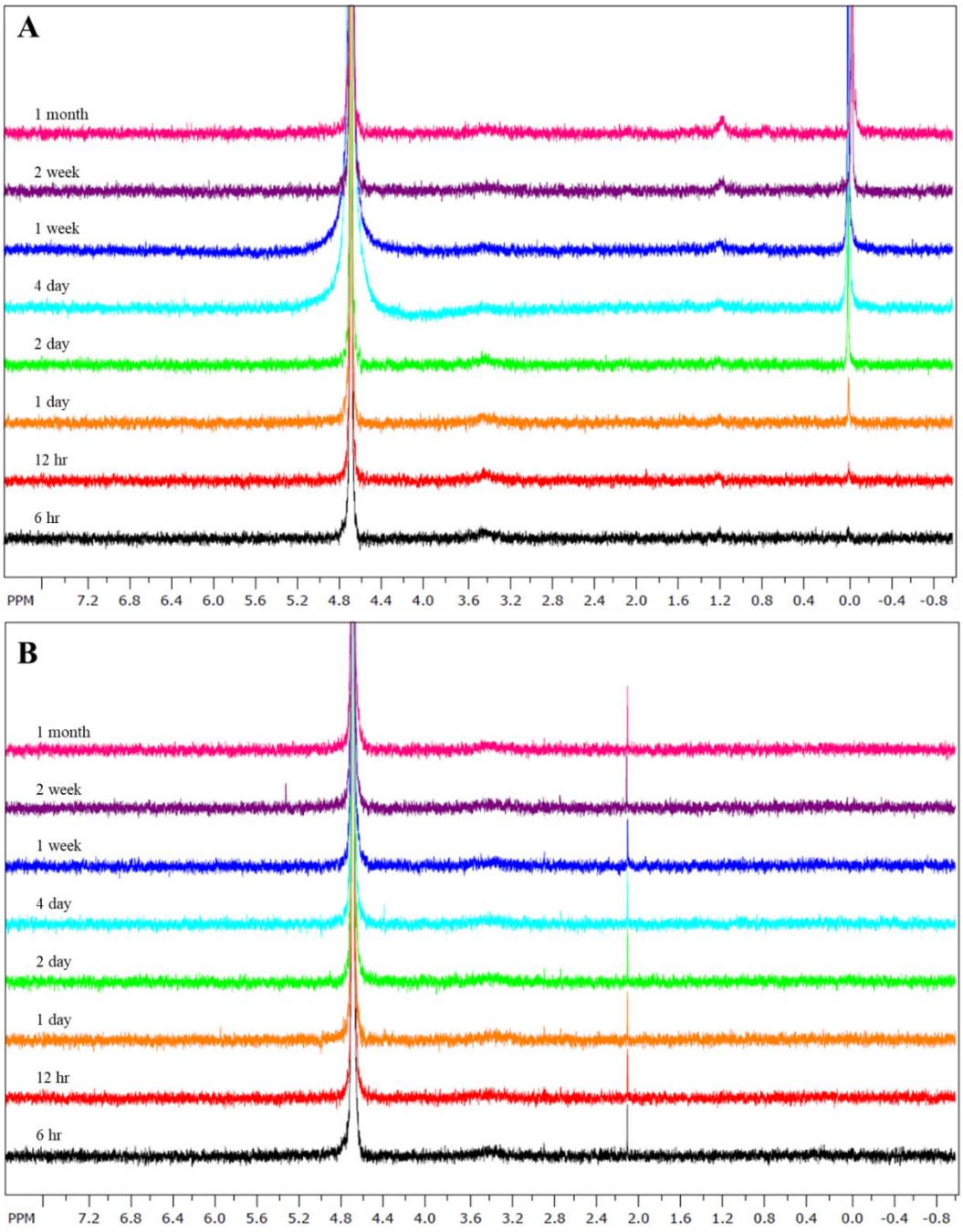

Figure S4: Leachability of samples into aqueous medium. **(A)** ^{1}H-NMR of aqueous extract from a commercial silicone gel used in breast implants monitored over a month (400 MHz, $CDCl_3$): 4.70 (Residual H_2O), 1.17, 0.01 (unidentified extract). **(B)** ^{1}H-NMR of aqueous extract from a 300-1/70 sample monitored over a month (400 MHz, D_2O): 4.70 (Residual H_2O), 2.09 (Residual acetone).

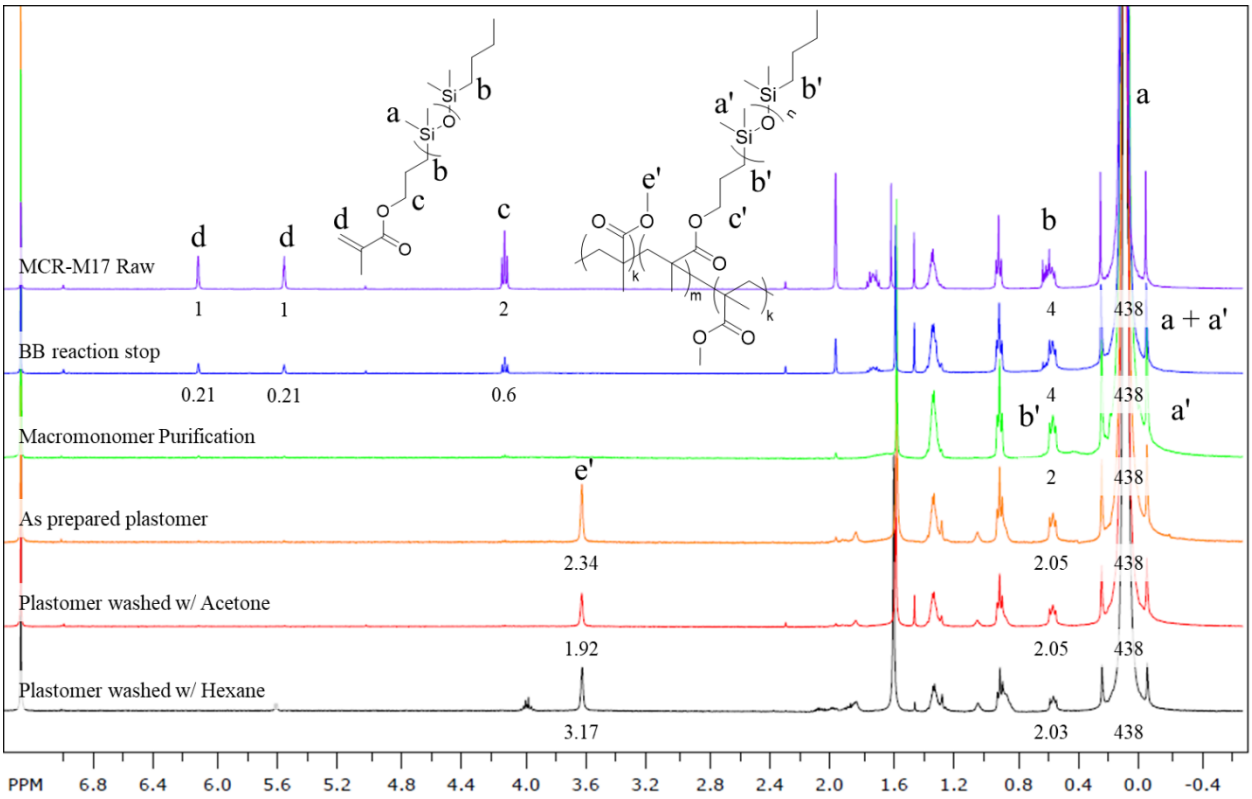

Figure S5: ^{1}H-NMR of LBL plastomer at different stages of synthesis. (400 MHz, $CDCl_3$): 6.12, 5.57 (CH_2=C(CH_3)C=O, PDMS macromonomer, s, 1H), 4.12 (CO-OCH_2-, PDMS macromonomer, t, 2H), 0.55 (-CH_2-(Si(CH_3)$_2$-O)$_n$-CH_2-CH_2-, PDMS macromonomer and bottlebrush mixture, m, 4H) 0.09 (-(Si(CH_3)$_2$-O)$_n$-, PDMS macromonomer and bottlebrush mixture, s, 438H). $Conv_{PDMS} = ([Area(a + a')/438] - [Area(d)/1])/[Area(a)/438]$ = 79%. Peaks c' and 1 set of 2H b' for bottlebrushes with n_{sc} = 70 do not show on NMR in $CDCl_3$ in contrast to n_{sc} = 14 bottlebrushes. For PMMA-PDMS-PMMA plastomer (400 MHz, $CDCl_3$): 3.62 (COO-CH_3, s, 3H), 0.55 (-CH_2-(Si(CH_3)$_2$-O)$_n$-CH_2-CH_2-, m, 2H) 0.09 (-Si(CH_3)$_2$-, s, 438H). $n_L = [Area(e')/3]/[Area(a)/438] * n_{bb}$ where $n_{bb} = Conv_{PDMS} * \frac{[M]}{[I]} = 79\% * 375 = 296$. Subsequent washing with PDMS anti-solvent acetone and PMMA anti-solvent hexane yields acetone soluble PMMA homopolymer and hexane soluble PDMS bottlebrush respectively.

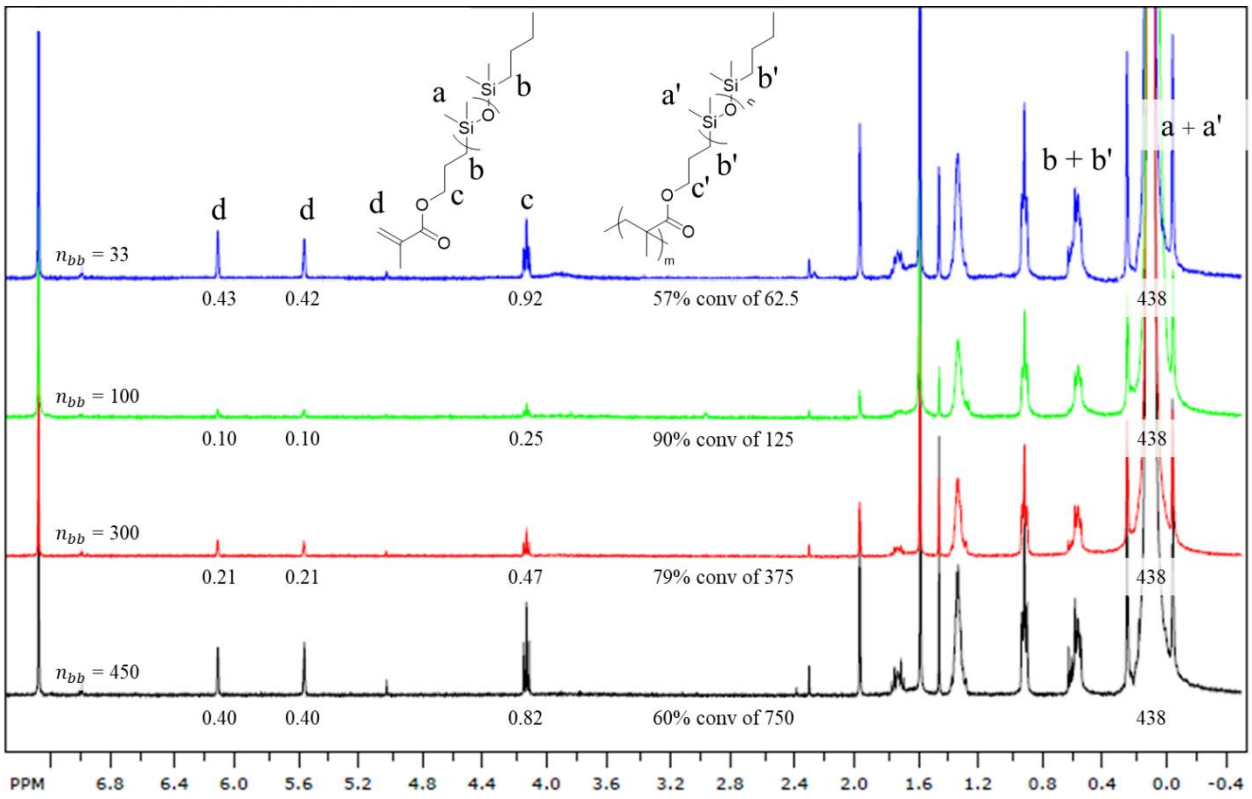

Figure S6: ^{1}H-NMR of PDMS bottlebrush B-blocks**.** Unpurified growth of n_{sc} = 70 PDMS brushes (400 MHz, $CDCl_3$): 6.12, 5.57 (C**H**$_2$=C(CH_3)C=O, PDMS macromonomer, s, 1H), 4.12 (CO-OC**H**$_2$-, PDMS macromonomer, t, 2H), 0.55 (-CH_2-($Si(CH_3)_2$-O)$_n$-C**H**$_2$-CH_2-, PDMS macromonomer and bottlebrush mixture, m, 2H) 0.09 (-(Si(C**H**$_3$)$_2$-O)$_n$-, PDMS macromonomer and bottlebrush mixture, s, 438H). For series 300-x/70, $Conv_{PDMS} = ([Area(a + a')/438] - [Area(d)/1])/[Area(a)/438]$ = 79% ; $n_{bb} = Conv_{PDMS} * \frac{[M]}{[I]} = 79\% * 375 = 296$.

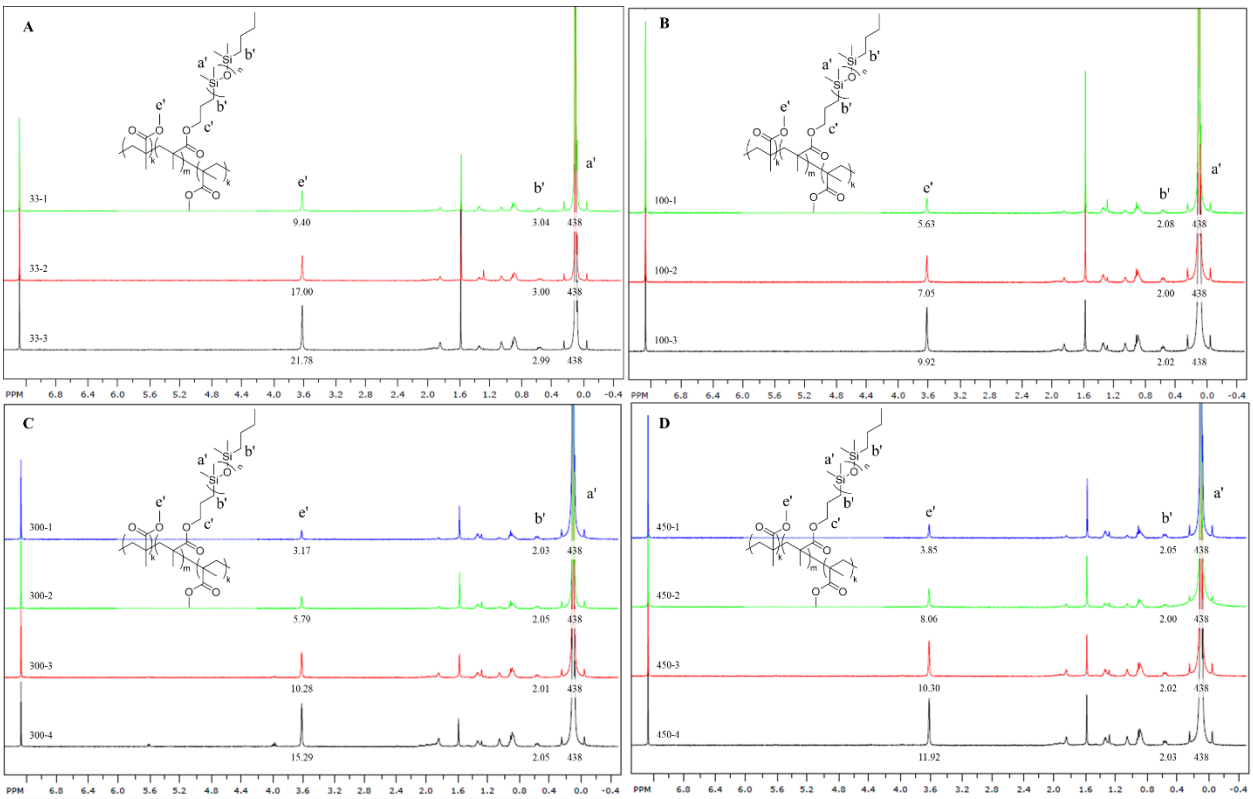

Figure S7: ^{1}H-NMR of LBL PMMA-PDMS-PMMA triblock copolymers. (400 MHz, $CDCl_3$): 3.62 (COO-C**H**$_3$, s, 3H), 0.55 (-CH$_2$-(Si(CH$_3$)$_2$-O)$_n$-C**H**$_2$-CH$_2$-, m, 2H) 0.09 (-Si(C**H**$_3$)$_2$-, s, 438H). $n_L = [Area(e')/3]/[Area(a')/438] * n_{bb}$. **(A)** 33-x/70 series **(B)** 100-x/70 series **(C)** 300-x/70 series **(D)** 450-x/70 series.

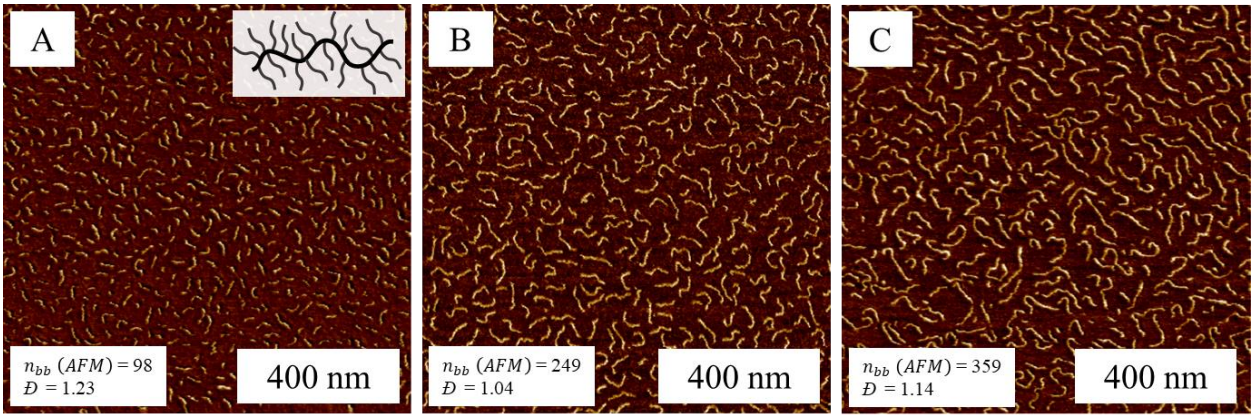

Figure S8: Atomic Force Microscopy of brush blocks. Height micrographs of PDMS bottlebrush blocks deposited on mica by Langmuir-Blodget technique for series **(A)** 100-x/70 **(B)** 300-x/70 **(C)** 450-x/70. Where n_{bb} is determined by AFM as L_n/l_0 where L_n is number average measured bottlebrush contour length via AFM and l_o= 0.25 nm is the length of bottlebrush backbone monomeric unit. Bottlebrush dispersity, Đ = M_w/M_n is calculated from analysis of > 300 molecules.

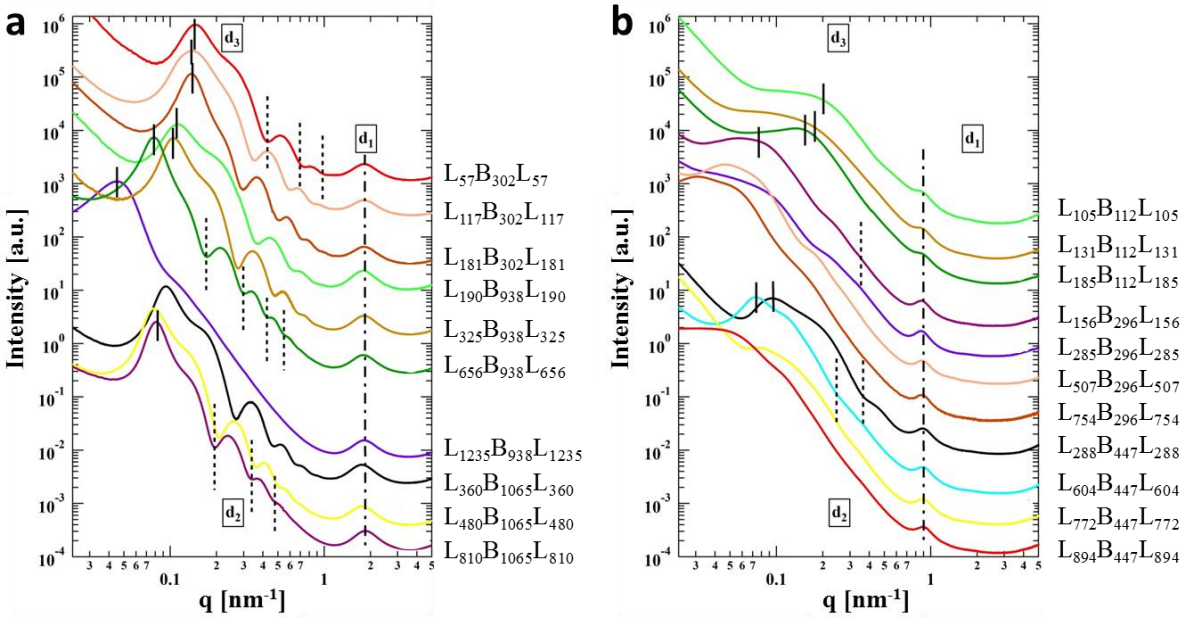

Figure S9: Composite of LBL X-ray spectra. **(a)** n_{sc} = 14 and **(b)** n_{sc} = 70 plastomers from **Table S3**.

REFERENCES

(34) Liang, H.; Wang, Z.; Dobrynin, A. V. Strain-adaptive self-assembled networks of linear-bottlebrush-linear copolymers. *Macromolecules* **2019**, *52*, doi:10.1021/acs.macromol.9b01859

(35) Place, E. S.; George, J. H.; Williams, C. K.; Stevens, M. Synthetic polymer scaffolds for tissue engineering. *Chem. Soc. Rev.* **2009**, *38*, 1139-1151.

(36) Maksym G. N.; Bates, J. H. A distributed nonlinear model of lung tissue elasticity. *J Appl. Physiol.* **1997**, *82*, 32-41.

(37) Pervin, F.; Chen, W. W. Effect of inter-species, gender, and breeding on the mechanical behavior of brain tissue. *NeuroImage* **2011**, *54*, S98-102.

(38) Holzapfel, G. A.; Sommer, G.; Regitnig, P. Anisotropic mechanical properties of tissue components in human atherosclerotic plaques. *J. Biomech. Eng.* **2004**, *126*, 657-665.

(39) Jabareen, M.; Mallik, A. S.; Bilic, G.; Zisch, A. H.; Mazza, E. Relation between mechanical properties and microstructure of human fetal membranes: an attempt towards a quantitative analysis. *Eur. J. Obstet. Gynecol. Reprod. Biol.* **2009**, *144*, 5134-5141.

(40) Kra, S.; Andreassen, T. T. Mechanical properties of human lens capsule. *Prog. Retin. Eye Res.* **2003**, *22*, 749-767.

(41) Chen, Q.-Z. Harding, S. E.; Ali, N. N.; Lyon, A. R.; Boccaccini, A. R. Biomaterials in cardiac tissue engineering: ten years of research survey. *Mater. Sci. Eng. R Rep.* **2008**, *59*, 1-37.

(42) Silver, F. H.; Freeman, J. W.; Devore, D. Viscoelastic properties of human skin and processed dermis. *Skin Res. Tech.* **2001**, *7*, 18-23.

(43) Hebrank, M. R. Mechanical properties and locomotor functions of eel skin. *Biol. Bull.* **1980**, *158*, 58-68.

(44) Bancelin, S.; Lynch, B.; Bonod-Bidaud, C.; Ducourthial, G.; Psilodimitrakopoulos, S.; Dokladal, P; Allain, J. M.; Schanne-Klein, M. C.; Ruggiero F. Ex vivo multiscale quantitation of skin biomechanics in wild-type and genetically-modified mice using multiphonon microscopy. *Sci. Rep.* **2015**, *5*, 17635.

(45) Lim, J.; Hong, J.; Chen, W.W.; Weerasooriya, T. Mechanical response of pig skin under dynamic tensile loading. *Int. J. Impact. Eng.* **2011**, *38*, 130-135.

(46) Chen, Z.-L.; Chen, Y.-Z.; Hu, Z.-Y. A micromechanical model for estimating alveolar wall strain in mechanically ventilated edematous lungs. *J. Appl. Physiol.* **2014**, *117*, 586-592.

(47) Hunter, E. J.; Titze, I. R. Refinements in modeling the passive properties of laryngeal soft tissue. *J. Appl. Physiol.* **2017**, *103*, 206-219.

(48) Wright, D. M.; Duance, V. C.; Wess, T. J.; Kielty, C. M.; Purslow, P. P. The supramolecular organisation of fibrillin-rich microfibrils determines the mechanical properties of bovine zonular filaments. *J. Exp. Bio.* **1999**, *202*, 3011-3020.

(49) Brown, S. H.; Carr, J. A.; Ward, S. R.; Lieber, R. L. Passive mechanical properties of rat abdominal wall muscles suggest an important role of the extracellular connective tissue matrix. *J. Orthop. Res.* **2012**, *30*, 1321-1326.

(50) Malisoux, L.; Francaux, M.; Nielens, H.; Theisen, D. Stretch-shortening cycle exercise: an effective training paradigm to enhance power output of human single muscle fibers. *J. Appl. Physiol.* **2006**, *100*, 771-779.

(51) Roberts, T. J. Contribution of elastic tissues to the mechanics and energetics of muscle function during movement. *J. Exp. Biol.* **2016**, *219*, 266-275.

(52) Alkhouli, N.; Mansfield, J.; Green, E.; Bell, J.; Knight, B.; Liversedge, N.; Tham, J. C.; Welbourn R.; Shore, A. C.; Kos, K.; Winlove, C. P. The mechanical properties of human adipose tissues and their relationships to the structure and composition of the extracellular matrix. *Am. Physiol. Soc.* **2013**, *305*, E1427-E1435.

(53) Zhou, B.; Xu, F.; Chen, C. Q. Strain rate sensitivity of skin tissue under thermomechanical loading. *Phil. Trans. R. Soc.* **2010**, *368*, 679-690.

(54) Holzapfel, G. A.; Sommer, G.; Gasser, C. T.; Regitnig, P. Determination of layer-specific mechanical properties of human coronary arteries with nonatherosclerotic intimal thickening and related constitutive modeling. *Am. J. Physiol. Heart Circ. Physiol.* **2005**, *289*, H2048-H2058.

(55) Abdelgaied, A.; Stanley, M.; Galfe, M.; Berry, H.; Ingham, E.; Fisher, J. Comparison of biomechanical tensile and compressive properties of decellularised and natural porcine meniscus. *J. Biomech.* **2015**, *48*, 1389-1396.

(56) Rausch, M. K.; Humphrey, J. D. A microstructurally inspired damage model for early venous thrombus. *J. Mech. Behav. Biomed. Mater.* **2015**, *55*, 12-20.

(57) Yang, T. Zhang, C.-q.; Liu, Q.; Li, K.; Yang, X.-p.; Zhang, J.-j. Hu, Y.; Ye, J. The rule of strain in different stratification of the intervertebral disc under physiologic loading. *Biomed. Res.* **2017**, *28*.

(58) Shreiber, D. I.; Hao, H.; Elias, R. A. Probing the influence of myelin and glia on the tensile properties of the spinal cord. *Biomech. Model. Mechanobiol.* **2009**, *8*, 311-321.

(59) Rashid, B.; Destrade, M.; Gilchrist, M. D. Mechanical characterization of brain tissue in tension at dynamic strain rates. *J. Mech. Behav. Biomed. Mater.* **2014**, *33*, 43-54.

(60) Ning, J.; Li, G.; Haraguchi, K. Synthesis of highly stretchable, mechanically tough, zwitterionic sulfobetaine nanocomposite gels with controlled thermosensitivities. *Macromolecules* **2013**, *46*, 5317-5328.

(61) Tan, M.; Zhao, T.; Huang, H.; Guo, M. Highly stretchable and resilient hydrogels from the copolymerization of acrylamide and a polymerizable macromolecular surfactant. *Poly. Chem.* **2013**, *4*, 5570-5576.

(62) Mithieux, S. M.; Rasko, J. E.; Weiss, A. S. Synthetic elastin hydrogels derived from massive elastic assemblies of self-organized human protein monomers. *Biomaterials* **2004**, *25*, 4921-4927.

(63) Carlsson, L.; Rose, S.; Hourdet, D.; Marcellan, A. Nano-hybrid self-crosslinked PDMS/silica hydrogels. *Soft Matter*, **2010**, *6*, 3619-3631.

(64) Feig, V. R.; Tran, H.; Lee, M.; Bao, Z. Mechanically tunable conductive interpenetrating network hydrogels that mimic the elastic moduli of biological tissue. *Nature Comm.* **2018**, *9*, 2740.

(65) Gong, J. P.; Katsuyama, Y.; Kurokawa, T.; Osada, Y. Double-Network hydrogels with extremely high mechanical strength. *Adv. Mater.* **2003**, *15*, 1155-1158.

(66) Haraguchi, K.; Takehisa, T. Nanocomposite hydrogels: a unique organic-inorganic network structure with extraordinary mechanical, optical and swelling/de-swelling properties. *Adv. Mater.* **2002**, *14*, 1120-1124.

(67) Kondo, S.; Sakurai, H.; Chug, U.; Sakai, T. Mechanical properties of polymer gels with bimodal distribution in stand length. *Macromolecules* **2013**, *46*, 7027-7033.

(68) Ohmori, K.; Bin, I. A.; Seki, T.; Liu, C.; Mayumi, K.; Ito, K.; Takeoka, Y. Molecular weight dependency of polyrotaxane cross-lined polymer gel extensibility. *Chem. Commun.* **2016**, *52*, 13757.

(69) Liu, Y.; Zhu, M.; Liu, X.; Zhang, W.; Sun, B.; Chen, Y.; Adler, H.-J. P. High clay content nanocomposite hydrogels with surprising mechanical strength and interesting deswelling kinetics. *Polymer* **2006**, *47*, 1-5.

(70) Xiong, L.; Hu, X.; Liu, X.; Tong, Z. Network chain density and relaxation of in situ synthesized polyacrylamide/ hectorite clay nanocomposite hydrogels with ultrahigh tensibility. *Polymer* **2008**, *49*, 5064-5071.

(71) Yano, S.; Mori, M.; Teramoto, N.; Lisaka, M.; Suzuki, N.; Noto, M.; Kaimoto, Y.; Kakimoto, M.; Yamada, M.; Shiratsuchi, E.; Shimasaki, T.; Shibata, M. Preparation of photocrosslinked fish elastin polypeptide/microfibrillated cellulose composite gels with elastic properties for biomaterial applications. *Mar. Drugs* **2015**, *13*, 338-353.

(72) Yuan, N.; Xu, L.; Wang, H.; Fu, Y.; Zhang, Z.; Liu, L.; Wang, C.; Zhao, J.; Rong, J. Dual physically cross-linked double network hydrogels with high mechanical strength, fatigue resistance, notch-insensitivity, and self-healing properties. *ACS Appl. Mater. Interfaces* **2016**, *8*, 34034-34044.

(73) Bakarich, S. E.; Panhuis, M.; Beirne, S.; Wallace, G. G.; Spinks, G. M. Extrusion printing of ionic-covalent entanglement hydrogels with high toughness. *J. Mater. Chem. B* **2013**, *1*, 4939-4946.

(74) Li, J. Illeperuma; W. R. K.; Suo, Z.; Vlassak, J. J. Hybrid hydrogels with extremely high stiffness and toughness. *ACS Macro Lett.* **2014**, *3*, 520-523.

(75) Yang, C. H.; Wang, M. X.; Haider, H.; Yang, J. H.; Sun, J.-Y.; Chen, Y. M.; Zhou, J.; Suo, Z. Strengthening alginate/polyacrylamide hydrogels using various multivalent cations. *ACS Appl. Mater. Interfaces* **2013,** *5*, 10418-10422.

(76) Lu, X.; Chan, C. Y.; Lee, K. I.; Ng, P. F.; Fei, B.; Xin, J. H.; Fu, J. Super-tough and thermo-healable hydrogel promising for shape-memory absorbent fiber. *J. Mater. Chem. B* **2014**, *2*, 7631-7638.

(77) Li, J.; Suo, Z.; Vlassak, J. J. Stiff, strong and tough hydrogels with good chemical stability. *J. Mater. Chem. B* **2014**, *2*, 6708-6713.

(78) Yue, Y. F.; Haque, M. A.; Kurokawa, T.; Nakajima, T.; Gong, J. P. Lamellar hydrogels with high toughness and ternary tunable photonic stop-band. *Adv. Mater.* **2013**, *25*, 3106-3110.

(79) Cong, H. P.; Wang, P.; Yu, S.-H. Stretchable and self-healing graphene oxide-polymer composite hydrogels: a dual-network design. *Chem. Mater.* **2013**, *25*, 3357-3362.

(80) Xin, H.; Saricilar, S. Z.; Brown, H. R.; Whitten, P. G.; Spinks, G. M. Effect of first network topology on the toughness of double network hydrogels. *Macromolecules* **2013**, *46*, 6613-6620.

(81) Es-haghi, S. S.; Leonov, A. I.; Weiss, R. A. Deconstructing the double-network hydrogels: the importance of grafted chains for achieving toughness. *Macromolecules* **2014**, *47*, 4769-4777.